metals

MDPI

Article

The Mechanism of Inhibiting the Adsorption of Rare-Earth Inclusions in Molten Steel by Al_2O_3, $YAlO_3$ and Y_2O_3 Refractory by Impressed Current

Xiaonan Zheng [1,2], Diqiang Luo [3,*], Chaobin Lai [1,2,*], Hebin Wang [4] and Chao Pan [1]

[1] School of Metallurgical Engineering, Jiangxi University of Science and Technology, Ganzhou 341000, China; 15985722003@163.com (X.Z.)
[2] Gannan Laboratory, Ganzhou 341000, China
[3] Jiangxi Provincial Key Laboratory of Particle Technology, Jiangxi University of Science and Technology, Nanchang 330013, China
[4] School of Materials Science and Engineering, Jiangxi University of Science and Technology, Ganzhou 341000, China
* Correspondence: luodiqiang@jxust.edu.cn (D.L.); 18907977225@163.com (C.L.)

Abstract

The adsorption of rare-earth Y-based inclusions (Y, Y_2O_3, Y_2O_2S) on Al_2O_3, $YAlO_3$, and Y_2O_3 refractory surfaces is a primary cause of nozzle clogging during the continuous casting of rare-earth steels. Conventional anti-clogging strategies, being passive and offline, lack real-time adjustability. This study aims to elucidate the mechanism by which external positive charge modulates interfacial adsorption. Using first-principles calculations combined with partial density of states, charge density difference, and thermodynamic analyses, we investigated the adsorption behavior of Y, Y_2O_3, and Y_2O_2S on Al_2O_3 (001), $YAlO_3$ (001), and Y_2O_3 (001) surfaces under neutral and positively charged states (+2, +4). A triple inhibition mechanism is revealed: electronically, external charge disrupts O-p and Y-d orbital hybridization, attenuating interfacial covalent bonding; electrostatically, the net positive charge shifts the interfacial interaction from attraction to repulsion, creating a physical barrier; and thermodynamically, the Gibbs free energy change ΔG increases under charged conditions, indicating a quantifiable reduction in adsorption spontaneity. These findings provide a theoretical basis for the development of active anti-clogging strategies in rare-earth steel production.

Keywords: rare-earth steel; nozzle clogging; applied current; adsorption; inhibition mechanism

Check for updates

Academic Editor: Srecko Stopic

Received: 15 February 2026
Revised: 28 March 2026
Accepted: 28 March 2026
Published: 9 April 2026

Copyright: © 2026 by the authors. Licensee MDPI, Basel, Switzerland. This article is an open access article distributed under the terms and conditions of the Creative Commons Attribution (CC BY) license.

1. Introduction

Rare-earth elements serve as critical microalloying components in the production of high-performance weathering steels, playing essential roles in purifying non-metallic inclusions, refining grain structures, and optimizing mechanical properties [1,2]. Among these, yttrium (Y) and its inclusions—particularly Y_2O_3 and Y_2O_2S (yttrium oxysulfide)—are widely utilized in advanced steel grades for high-speed rail and nuclear power applications [3,4]. However, during continuous casting, these Y-based species readily adsorb onto Al_2O_3, $YAlO_3$, and Y_2O_3 refractory nozzle surfaces, gradually accumulating and causing flow channel blockage within several hours [5]. Industry statistics indicate that a single clogging incident can result in economic losses exceeding hundreds of thousands of RMB, with annual losses for rare-earth steel production reaching tens of millions [6].

As demand for rare-earth microalloyed steels continues to surge, this issue has evolved from an occasional operational disturbance into a critical bottleneck constraining the stable production of high-end steel grades [7].

Conventional anti-clogging strategies primarily encompass alloy modification, protective coatings, and flow field optimization [8,9]. Alloying with calcium modifies alumina inclusions into low-melting liquid phases, while coatings such as BN or ZrO_2-C are applied to refractory surfaces as physical barriers [10,11]. Although these approaches have demonstrated efficacy under specific conditions, they fundamentally represent passive, offline countermeasures [12,13]. Their protective performance becomes fixed upon nozzle installation, precluding dynamic adjustment in response to steel composition variations and rendering active intervention during early clogging stages impossible [14,15]. With accelerating casting speeds and increasing fluctuations in rare-earth addition, the limitations of conventional techniques have become increasingly pronounced [16,17].

External electric current modulation has recently emerged as a promising active strategy to overcome these inherent limitations [18,19]. By applying a weak electric current to the refractory surface, a responsive "intelligent barrier" can be established in real time, enabling millisecond-level, continuous, and reversible control of adsorption strength [20]. This approach currently represents one of the few anti-clogging strategies possessing genuine dynamic tunability [21]. Nevertheless, the fundamental scientific question underlying this technology—namely, how electric current modulates interfacial adsorption behavior from atomic and electronic perspectives—remains largely unexplored, persisting as a "black box" [22]. Critical aspects, including electron transfer pathways, orbital reconstruction mechanisms, bond disruption modes, and thermodynamic driving force alterations, lack systematic elucidation [19]. Consequently, electrochemical anti-clogging techniques have remained confined to empirical experimentation without robust theoretical guidance [23].

In this work, we employ first-principles calculations based on density functional theory to systematically investigate the influence of external positive charge on the adsorption behavior of Y, Y_2O_3, and Y_2O_2S on Al_2O_3 (001), $YAlO_3$ (001), and Y_2O_3 (001) surfaces. Through integrated analysis of the partial density of states, charge density difference, and high-temperature thermodynamics, we reveal a triple inhibition mechanism involving orbital hybridization attenuation, electrostatic environment reversal, and thermodynamic driving force reduction. These findings elucidate the microscopic origin of charge-governed adsorption inhibition and provide a theoretical foundation for developing electrochemically inert anti-clogging interfaces in rare-earth steel continuous casting.

2. Materials and Methods

The calculations are performed under vacuum, neglecting the molten steel environment. The surfaces are modeled as ideal, defect-free (001) terminations, whereas real refractory surfaces contain steps, vacancies, and impurities. The applied charge states are introduced as a fixed electron addition, which is an idealization of the complex electrochemical environment. It should be noted that these simplifications were intentionally implemented to decouple the fundamental electronic mechanism governing charge-modulated adsorption, constituting an essential first step prior to the inclusion of additional complexity.

2.1. Establishment of Adsorption Structure Model

In this study, based on density functional theory (DFT), the calculation and analysis were carried out by using the Vienna first-principles simulation software package (VASP6.4.2). The electron exchange correlation effect is described by the Perdew–Burke–Ernzerhof (PBE) functional under the generalized gradient approxima-

tion (GGA), and the ion–electron interaction is treated by the projection augmented wave (PAW) method. The cutoff energy of plane wave expansion is set to 450 eV.

In the structural optimization of Al_2O_3, $YAlO_3$ and Y_2O_3 phase materials, $5 \times 5 \times 5$ and Monkhorst–Pack type $2 \times 2 \times 1$ k-point grids centered on Γ are used respectively. The atomic positions of all models are completely relaxed until the Hellmann–Feynman force converged to within 0.01 eV/Å, and the total energy change is less than 10^{-5} eV. In order to eliminate the interlayer interference caused by periodic boundary conditions, all surface models introduce a vacuum layer with a thickness of 15 Å in the vertical direction. In addition, in order to accurately describe the non-bond interaction in the adsorption interface, the DFT-D3 correction method proposed by Grimme was used to correct the van der Waals forces.

2.2. Calculation of Adsorption Energy

The adsorption energy (E_{ads}) of species is calculated by the following:

$$E_{ads} = E_{system} - E_{substrate} - E_{adsorbate} \quad (1)$$

where E_{system}, $E_{substrate}$, and $E_{adsorbate}$ are the total energy of the optimized system with adsorbed species, the energy of the clean slab, and the energy of the isolated adsorbate molecule.

2.3. Thermodynamic Calculation

To evaluate the zero-point energy (ZPE) and vibrational entropy (S_{vib}) contributions, phonon calculations were performed using the Phonopy2.40.0 code interfaced with VASP. Phonon frequencies were obtained via the finite displacement method, in which all atoms were displaced by 0.01 Å from their equilibrium positions. The force constants were calculated based on the Hellmann–Feynman forces with a convergence criterion of 10^{-6} eV/Å to ensure numerical accuracy. The ZPE and S_{vib} were then evaluated within the harmonic approximation using the standard statistical thermodynamic relations:

$$ZPE = \frac{1}{2}\sum_i h\nu_i \quad (2)$$

$$S_{vib} = k_B \sum_i \left[\frac{\hbar\omega i}{k_B T} \times \frac{1}{e^{\hbar\omega i/k_B T} - 1} - In\left(1 - e^{-\hbar\omega i/k_B T}\right) \right] \quad (3)$$

For gas-phase molecules, the translational and rotational entropy contributions were additionally considered using the ideal gas approximation, as implemented in the Phonopy code. The total entropy change ΔS for each adsorption process was calculated as the sum of the vibrational entropy change in the solid system and the translational/rotational entropy change in the gas-phase species.

The Gibbs free energy change (ΔG) for the adsorption processes was calculated using the following equation:

$$\Delta G = \Delta E + \Delta ZPE - T\Delta S \quad (4)$$

where ΔE is the electronic energy difference between the adsorption system and the isolated reactants (slab and adsorbate), obtained from DFT calculations performed with the Vienna Ab initio Simulation Package (VASP). The Perdew–Burke–Ernzerhof (PBE) functional within the generalized gradient approximation (GGA) was employed, together with the projector augmented wave (PAW) pseudopotential method. The DFT-D3 correction of Grimme was applied to account for van der Waals interactions.

The temperature range considered in this study spans from 1473.15 K to 1873.15 K, which corresponds to the typical continuous casting temperatures of rare-earth steels. All

thermodynamic quantities were obtained using the PBE + PAW framework with DFT-D3 dispersion correction.

2.4. Differential Charge Density Calculation

The charge density difference (CDD) was computed as follows:

$$\Delta\rho = \rho_{total} - \rho_{substrate} - \rho_{adsorbate} \quad (5)$$

where ρ_{total} is the charge density of the fully relaxed adsorption system, and $\rho_{substrate}$ and $\rho_{adsorbate}$ are the charge densities of the isolated substrate and adsorbate.

To ensure internal consistency, all three components—total system, isolated substrate, and isolated adsorbate—were computed using an identical supercell with fixed atomic coordinates. For charged systems carrying +2 |e| or +4 |e|, the total number of electrons was adjusted via the NELECT tag, and the same NELECT value was strictly maintained across all three components to preserve the validity of the charge density difference analysis. Isosurface representations of charge redistribution were rendered using VESTA at an isovalue of ± 0.001 e/Å^3.

2.5. Partial Density of States Calculation

Projections of the partial density of states (PDOSs) onto specific atomic orbitals—namely O-p, Y-d, and Y-s—were obtained from self-consistent charge densities using the LORBIT = 11 tag, which decomposes wave functions into spherical harmonics within the PAW spheres. All PDOS profiles were smoothed using a Gaussian broadening function with a width of 0.05 eV, and the Fermi level was uniformly aligned to zero across all systems. For charged configurations (+2 and +4), identical NELECT parameters employed in the CDD calculations were reused to ensure electronic structure comparability under equivalent charge backgrounds. The orbital-resolved PDOS spectra were subsequently analyzed to assess energy alignment, peak mirroring behavior, and hybridization trends between Y-d/Y-s and O-p orbitals as a function of the charge state.

2.6. Ab Initio Molecular Dynamics (AIMD) Simulations

AIMD simulations were performed to investigate the dynamic adsorption behavior under thermal conditions. A time step of 1 fs was used throughout all simulations, and the temperature was maintained at 1830 K using a Nosé–Hoover thermostat. The bottom layer of the substrate was fixed, while a 10 nm vacuum layer was added in the z-direction to eliminate periodic boundary effects. Adsorbates (Y, Y_2O_3, and Y_2O_2S) were randomly placed in a region 4–5 nm above the substrate and allowed to fall onto the surface under thermal motion.

To evaluate the effect of electric charge on adsorption, each substrate was assigned one of three charge states (0, +2, and +4). A total of 45 independent simulations were carried out, covering 5 substrates, 3 adsorbates, and 3 charge states, with each simulation lasting 1 ns. During the simulations, structural evolution was recorded, and key parameters such as the number of interfacial adsorbed species, radial distribution function (RDF) and coordination number (CN) were calculated for analysis.

3. Results and Discussion

3.1. Adsorption Configuration Optimization

In this study, the adsorption behavior of rare-earth inclusions (Y atom, Y_2O_3, and Y_2O_2S) on Al_2O_3, $YAlO_3$ and Y_2O_3 (001) surfaces is investigated. For the (001) surfaces of Al_2O_3, $YAlO_3$ and Y_2O_3, three typical adsorption sites are investigated: the hollow site (H) located directly above the oxygen atom, the bridge site (B) located at the midpoint of the

Al–O or Y–O bond, and the top site (T) located directly above the Al or Y atom. Figures 1–3 show the initial adsorption configurations of the Y atom, Y_2O_3 and Y_2O_2S molecules on different substrates and the final structure after complete relaxation, respectively.

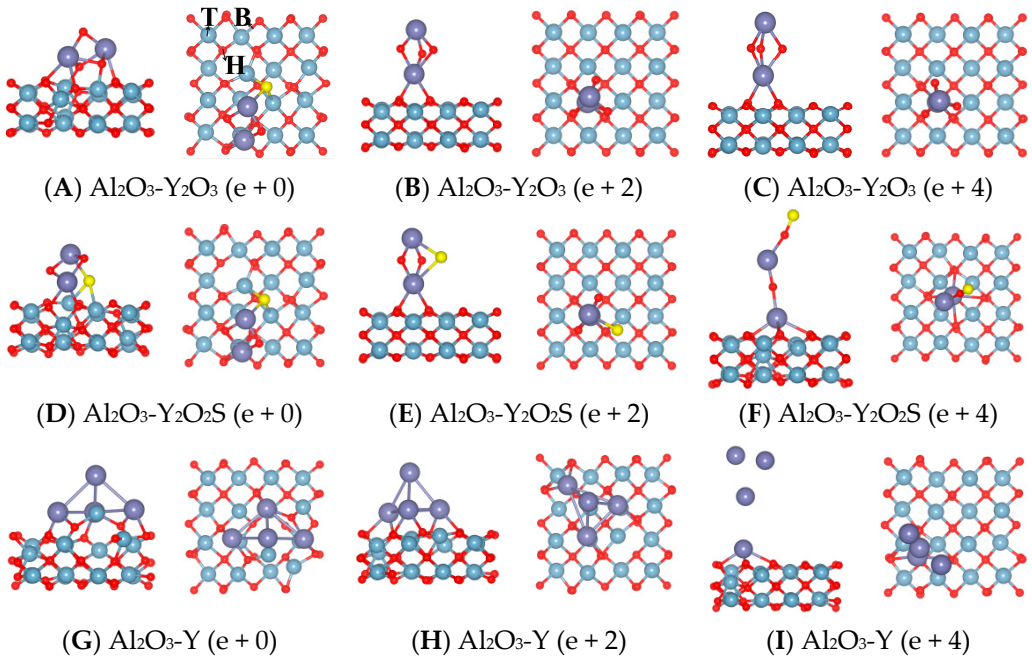


Figure 1. Structural shape of stable adsorption of Y, Y_2O_3 and Y_2O_2S on (001) surface of Al_2O_3 (red is O atom, blue is Al atom, yellow is S atom, and gray is Y atom.). (**A**–**C**) are the structures of Al_2O_3 adsorbing Y_2O_3 under the external charge of +0, +2 and +4, (**D**–**F**) are the structures of Al_2O_3 adsorbing Y_2O_2S under the external charge of +0, +2 and +4, (**G**–**I**) are the structures of Al_2O_3 adsorbing Y atom under the external charge of +0, +2 and +4.

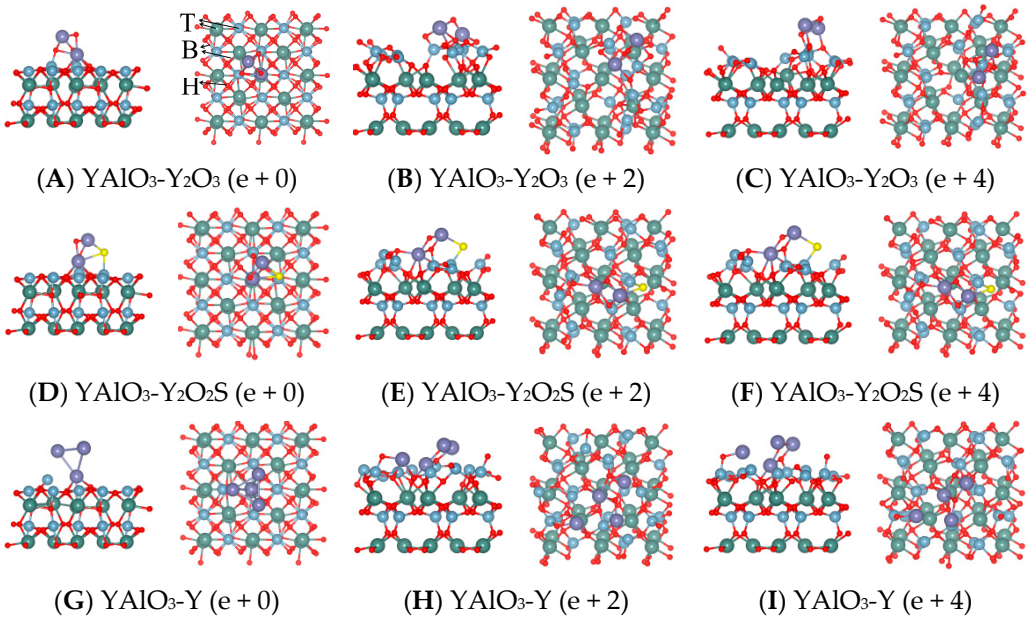


Figure 2. Structural shape of stable adsorption of Y, Y_2O_3 and Y_2O_2S on (001) surface of $YAlO_3$ (red is O atom, blue is Al atom, yellow is S atom, and green for Y atoms in the substrate, light gray for Y atoms in the adsorbates.). (**A**–**C**) are the structures of $YAlO_3$ adsorbing Y_2O_3 under the external charge of +0, +2 and +4, (**D**–**F**) are the structures of $YAlO_3$ adsorbing Y_2O_2S under the external charge of +0, +2 and +4, (**G**–**I**) are the structures of $YAlO_3$ adsorbing Y atom under the external charge of +0, +2 and +4.

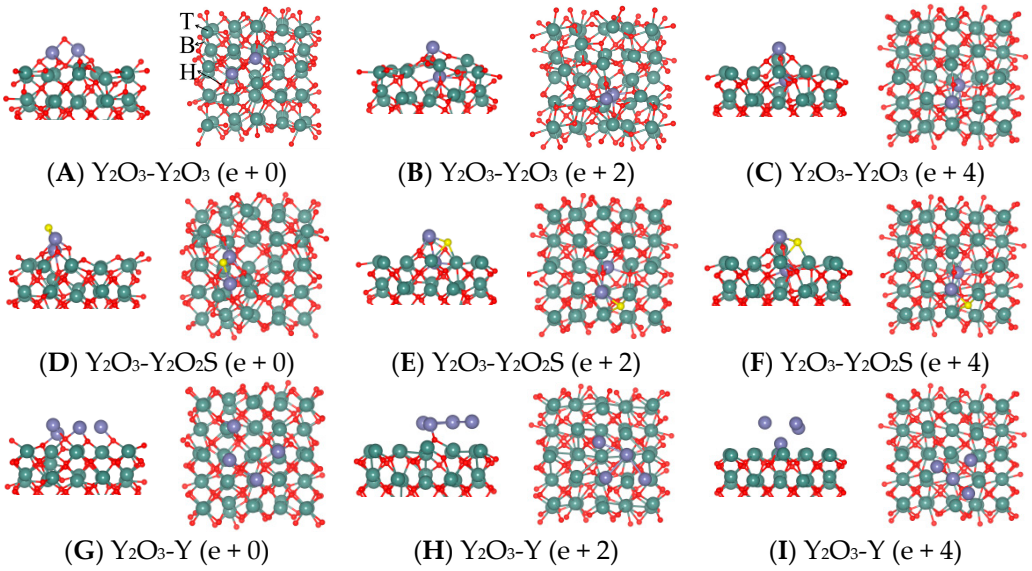


Figure 3. Structural shape of stable adsorption of Y, Y_2O_3 and Y_2O_2S on (001) surface of Y_2O_3 (red is O atom, yellow is S atom, and green for Y atoms in the substrate, light gray for Y atoms in the adsorbates.). (**A**–**C**) are the structures of Y_2O_3 adsorbing Y_2O_3 under the external charge of +0, +2 and +4, (**D**–**F**) are the structures of Y_2O_3 adsorbing Y_2O_2S under the external charge of +0, +2 and +4, (**G**–**I**) are the structures of Y_2O_3 adsorbing Y atom under the external charge of +0, +2 and +4.

By comparing the configuration changes before and after optimization, we observe that the adsorbed species initially located at the B-site or T-site migrate after structural relaxation, and finally tend to be located near the H-site. This phenomenon indicates that the H-site has a stronger adsorption affinity for rare-earth inclusions than the B- and T-sites, suggesting that the H-site is the stable site preferentially anchored on the refractory surface.

With the increase in the level of positive charge, the rare-earth inclusions gradually deviate from the substrate surface, indicating a trend of weakening adsorption or even desorption. It is worth noting that in the $YAlO_3$ system, the Al atoms in the crystal structure exhibit significant positional shifts, suggesting that charge application not only affects the adsorption behavior, but may also induce perturbation of the local structure of the substrate.

3.2. Adsorption Energy Analysis

Al_2O_3, $YAlO_3$ and Y_2O_3 exhibit distinct differences in adsorption energy when adsorbing the Y atom, Y_2O_3 and Y_2O_2S (Figure 4). For the adsorption of Y atoms, an increase in the surface positive charge of the three materials leads to a decrease in adsorption capacity. Taking Al_2O_3 as an example, when the surface charge is +0, the adsorption energy of Y is approximately −19 eV/mol, which is significantly higher than that under the +4 charge state. The response of Al_2O_3 to the applied charge is the most pronounced, while the adsorption strength of $YAlO_3$ and Y_2O_3 also decreases under a high charge, but the change trend is relatively gentle.

When Y_2O_3 and Y_2O_2S inclusions are adsorbed, the adsorption energy changes in the three materials exhibit a more moderate variation with an increase in charge. Overall, the adsorption capacity of Al_2O_3 for rare-earth inclusions is consistently stronger than that of $YAlO_3$ and Y_2O_3, while the adsorption capacity of Y_2O_3 is the lowest, and its adsorption energy exhibits the weakest response to charge variations.

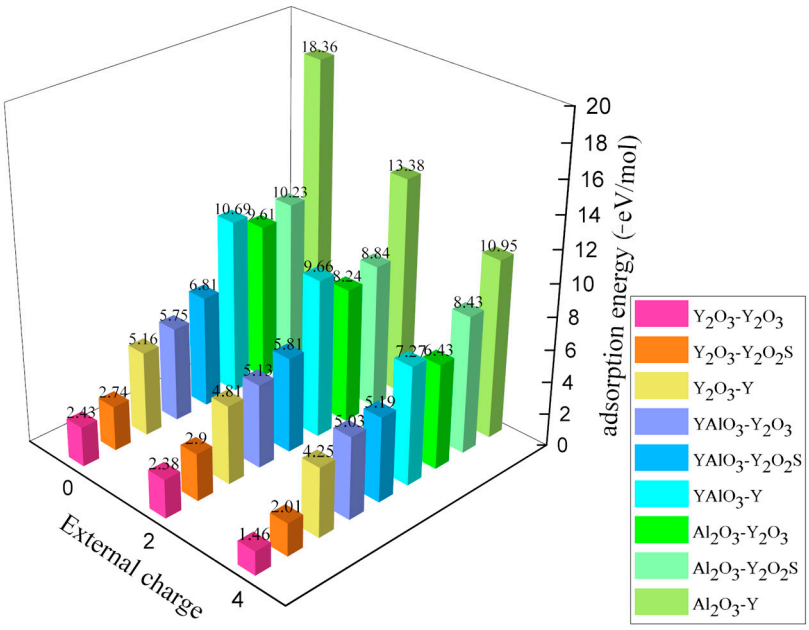
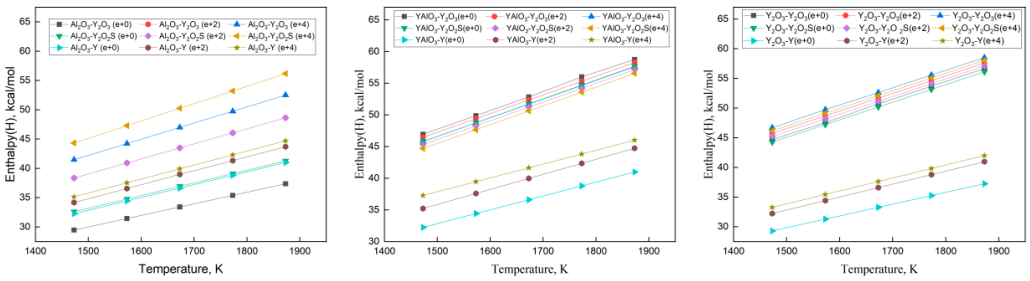


Figure 4. Adsorption energies of Al_2O_3, $YAlO_3$, and Y_2O_3 for Y, Y_2O_3 and Y_2O_2S.

An increase in surface charge may lead to an increase in the surface barrier of the substrate, thereby reducing the electrostatic interaction with the adsorbate and affecting the interaction mechanism between the interfaces. For Al_2O_3, the positive charge accumulation likely weakens the bonding interaction between the Al–O active site and Y on the surface, thereby reducing the adsorption energy. In the case of the adsorption of Y_2O_3 and Y_2O_2S, the adsorption energy of $YAlO_3$ and Y_2O_3 does not change significantly, indicating that the interface interaction between them and these inclusions is relatively stable and less affected by charge disturbance. Al_2O_3 exhibits a more pronounced change, which may be closely related to its higher surface chemical activity.

3.3. Thermodynamic Analysis of Charge-Modulated Adsorption

Figures 5 and 6 show the evolution of enthalpy (H) and entropy (S) of the adsorption systems as a function of temperature under different applied current conditions. In the temperature window from 1473 K to 1873 K, the enthalpy and entropy of all adsorption models increase linearly with the increasing temperature, but the change rate of entropy is relatively flat. This phenomenon indicates that above 1473 K, the effect of temperature on the adsorption entropy change gradually weakens, and adsorption behavior is no longer governed solely by temperature but is increasingly dominated by non-thermodynamic variables such as interfacial chemical potential, local charge state, and adsorption cluster size.



(**A**) (**B**) (**C**)

Figure 5. The enthalpy change curves of Al_2O_3, $YAlO_3$ and Y_2O_3 adsorption systems with temperature and charge ((**A**) is Al_2O_3, (**B**) is $YAlO_3$, (**C**) is Y_2O_3).

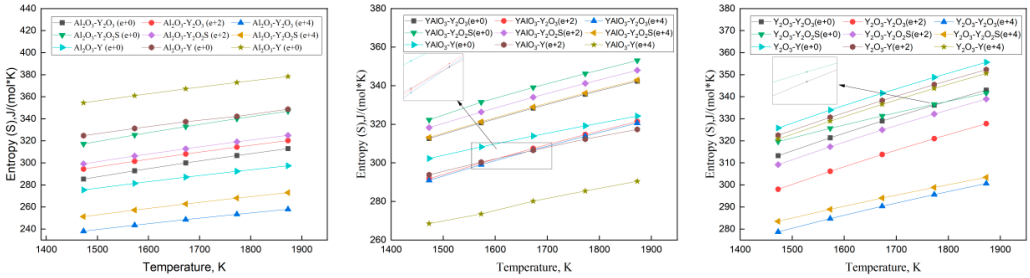


Figure 6. The curves of entropy of Al_2O_3, $YAlO_3$ and Y_2O_3 adsorption systems with temperature and charge change ((**A**) is Al_2O_3, (**B**) is $YAlO_3$, (**C**) is Y_2O_3).

Comparing the free energy changes in the adsorption system under different external charge states, we find that whether the adsorption species is Y_2O_3 and Y_2O_2S or Y atom, and whether the substrate material is Al_2O_3, $YAlO_3$ and Y_2O_3, the Gibbs free energy change (ΔG) in the adsorption reaction under the condition of applying +2 or +4 positive charge is significantly higher than the ΔG value of the uncharged (0) state (Figure 7). This trend carries a clear thermodynamic significance, indicating that the external positive charge can effectively weaken the spontaneity of the adsorption reaction, shifting the adsorption equilibrium toward dissociation, and reducing interfacial stability.

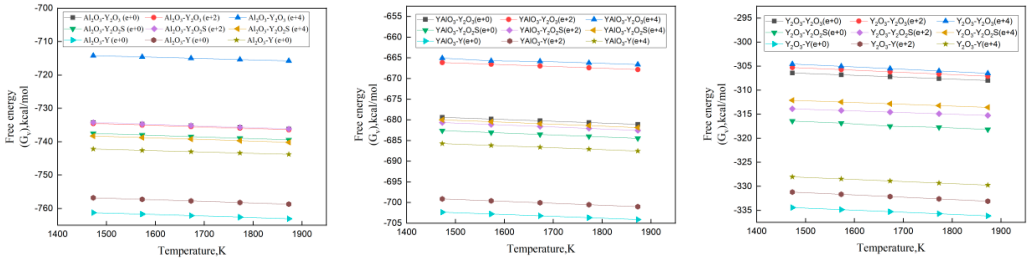


Figure 7. Gibbs free energy curves of Al_2O_3, $YAlO_3$, and Y_2O_3 adsorption systems versus temperature and external charge ((**A**) is Al_2O_3, (**B**) is $YAlO_3$, (**C**) is Y_2O_3).

It is worth noting that the inhibition effect suggests a consistent trend in different adsorption systems and different substrate materials, suggesting that the observed charge-induced inhibition may represent a general feature for Y-type inclusions on the oxide surface. This interpretation is consistent with previous theoretical work by Lousada et al. [24,25], who showed that surface charge significantly affects adsorption energetics across a range of oxide surfaces, and with experimental studies demonstrating potential-dependent adsorption on diverse oxide materials.

3.4. Formatting of Mathematical Components

Through the charge density difference analysis in Figures 8–10, we clearly observe that there is a significant charge directional migration between the Al_2O_3, $YAlO_3$ and Y_2O_3 substrates and the Y_2O_3 and Y_2O_2S or Y atom adsorbates in the steel. Specifically, electrons are transferred from the substrate side to the adsorbate side, forming an interface charge reconstruction pattern of "substrate electron loss–adsorbate electron gain". This charge redistribution feature highly suggests the electron density distribution of polar covalent bonds or ion–covalent mixed bonds, which provides direct evidence for the formation of interfacial chemical bonds.

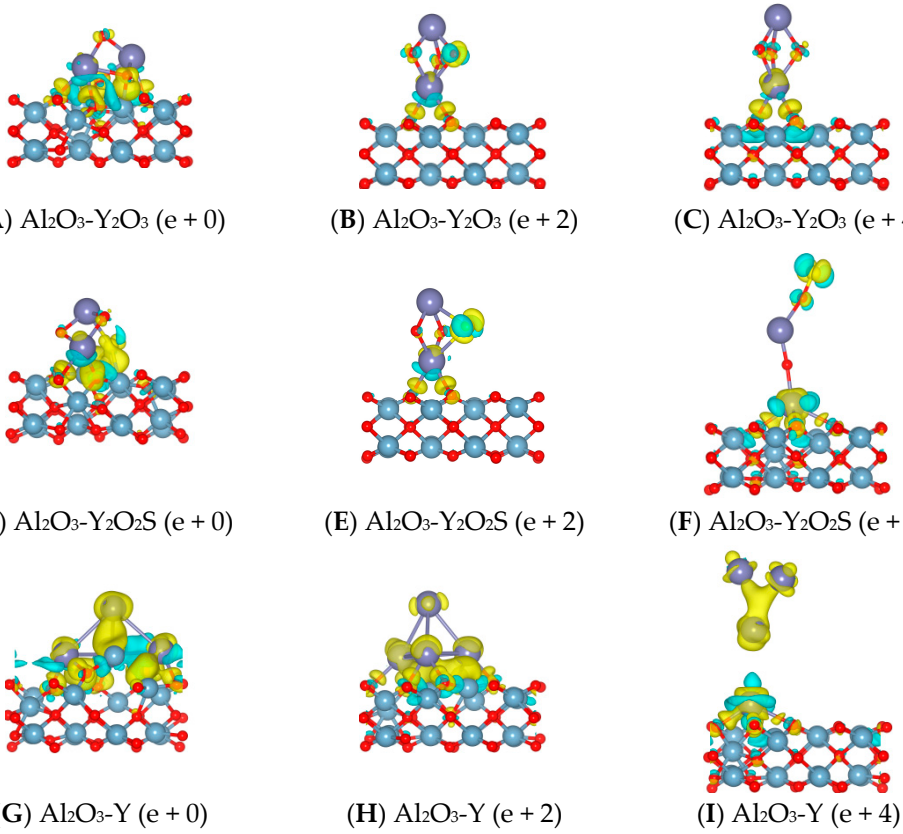


Figure 8. The charge density change in Al_2O_3 adsorption system; yellow is electron accumulation and cyan is electron dissipation. (**A**–**C**) are the differential charge structures of Al_2O_3 adsorbing Y_2O_3 under the external charge of +0, +2 and +4. (**D**–**F**) are the differential charge structures of Al_2O_3 adsorbing Y_2O_2S under the external charge of +0, +2 and +4. (**G**–**I**) are the differential charge structures of Al_2O_3 adsorbing Y atom under the external charge of +0, +2 and +4.

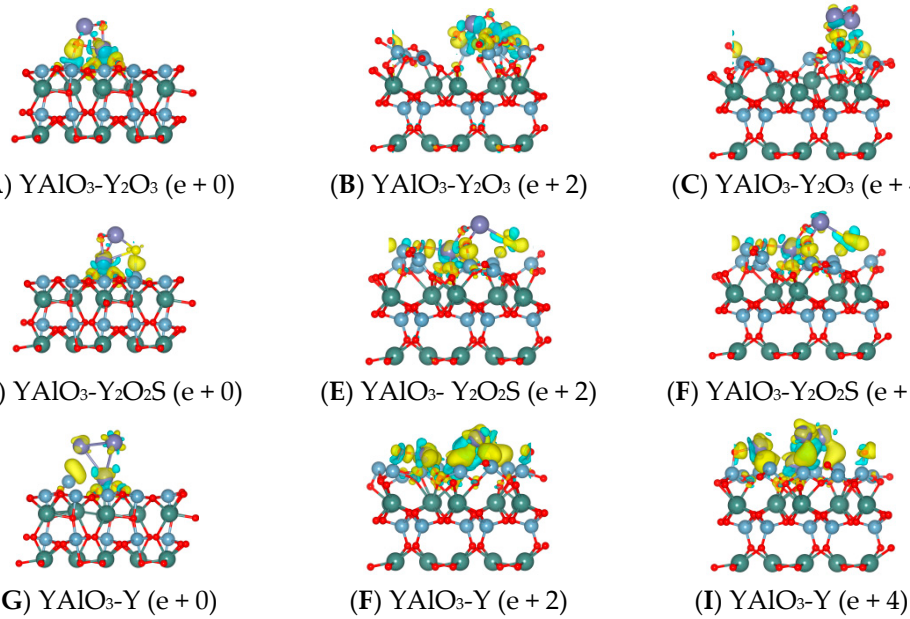


Figure 9. The charge density change in $YAlO_3$ adsorption system; yellow is electron accumulation and cyan is electron dissipation. (**A**–**C**) are the differential charge structures of $YAlO_3$ adsorbing Y_2O_3 under the external charge of +0, +2 and +4. (**D**–**F**) are the differential charge structures of $YAlO_3$ adsorbing Y_2O_2S under the external charge of +0, +2 and +4. (**G**–**I**) are the differential charge structures of $YAlO_3$ adsorbing Y atom under the external charge of +0, +2 and +4.

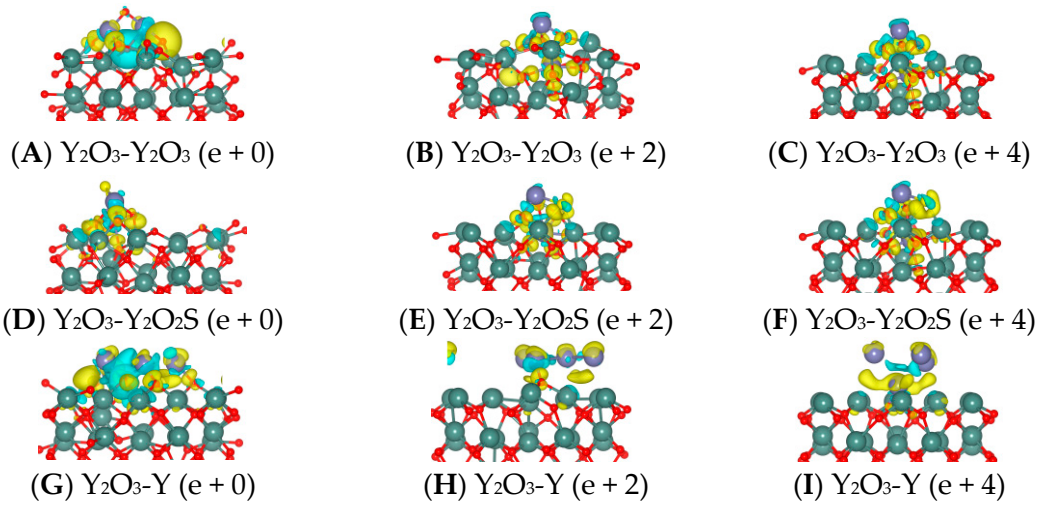


Figure 10. The charge density change in Y_2O_3 adsorption system; yellow is electron accumulation and cyan is electron dissipation. (**A**–**C**) are the differential charge structures of Y_2O_3 adsorbing Y_2O_3 under the external charge of +0, +2 and +4. (**D**–**F**) are the differential charge structures of Y_2O_3 adsorbing Y_2O_2S under the external charge of +0, +2 and +4. (**G**–**I**) are the differential charge structures of Y_2O_3 adsorbing Y atom under the external charge of +0, +2 and +4.

Further analysis shows that the magnitude and spatial distribution of charge transfer exhibit clear localization characteristics, and the electron dissipation and accumulation zone are not uniformly distributed but extend along specific atomic bonding directions. This distribution pattern indicates that the interface bond formed between the Y-based adsorbate and the O atom in the substrate exhibits strong directionality, reflecting the important role of covalent interactions.

As the external positive charge increases, the electron cloud density of oxygen atoms on the surface of the substrate generally decreases, along with a reduction in their nucleophilic activity. The extent of the electron depletion region on the substrate side in the charge density difference diagram is significantly reduced, indicating that the introduction of the overall positive charge background suppresses the electron supply capacity of the substrate, thereby weakening the interfacial charge transfer efficiency and the formation strength of chemical bonds. This phenomenon elucidates the electronic-level regulation mechanism of the external charge on the interface bonding behavior, and provides microscopic theoretical support for understanding the charge-induced adsorption inhibition.

3.5. Analysis of Partial Density of States

As shown in Figures 11–13, in the absence of external charges, there are obvious orbital coupling characteristics between the O atoms on the surface of Al_2O_3, $YAlO_3$ and Y_2O_3 and the Y_2O_3 and Y_2O_2S or Y atom adsorbates in the steel. Partial density of states analysis reveals that the O-p orbitals and the Y-d orbitals have significant PDOS peaks in the occupied states on both sides of the Fermi level. The peaks of the two are mirror-symmetric and fluctuate synchronously, indicating that the Y-d/O-p hybrid orbitals are formed at the interface, corresponding to the bonding states and the antibonding states, respectively, reflecting a strong covalent interaction.

When the positive charge of +2 is introduced, the electronic structure of the system changes significantly. In the occupied state region, the number and intensity of PDOS peaks increase, indicating that the original hybrid band becomes localized and energy level splitting, the effective mass of electrons increases, and the covalency has begun to decrease. In the unoccupied state region, the PDOS peaks corresponding to the antibonding states gradually weaken, indicating that the contribution of the Y-d orbital to the conduction band is partially suppressed. Notably, the Y-s orbital begins to appear at this stage and overlaps with the O-p orbital, suggesting that the enhancement in the effective nuclear charge of the Y atom causes the s orbital energy level to decrease and initiates its participation in bonding, indicating that the bonding mode may change. Meanwhile, the energy gap exhibits an incipient narrowing trend, and the main peak spacing near $E = 0$ decreases.

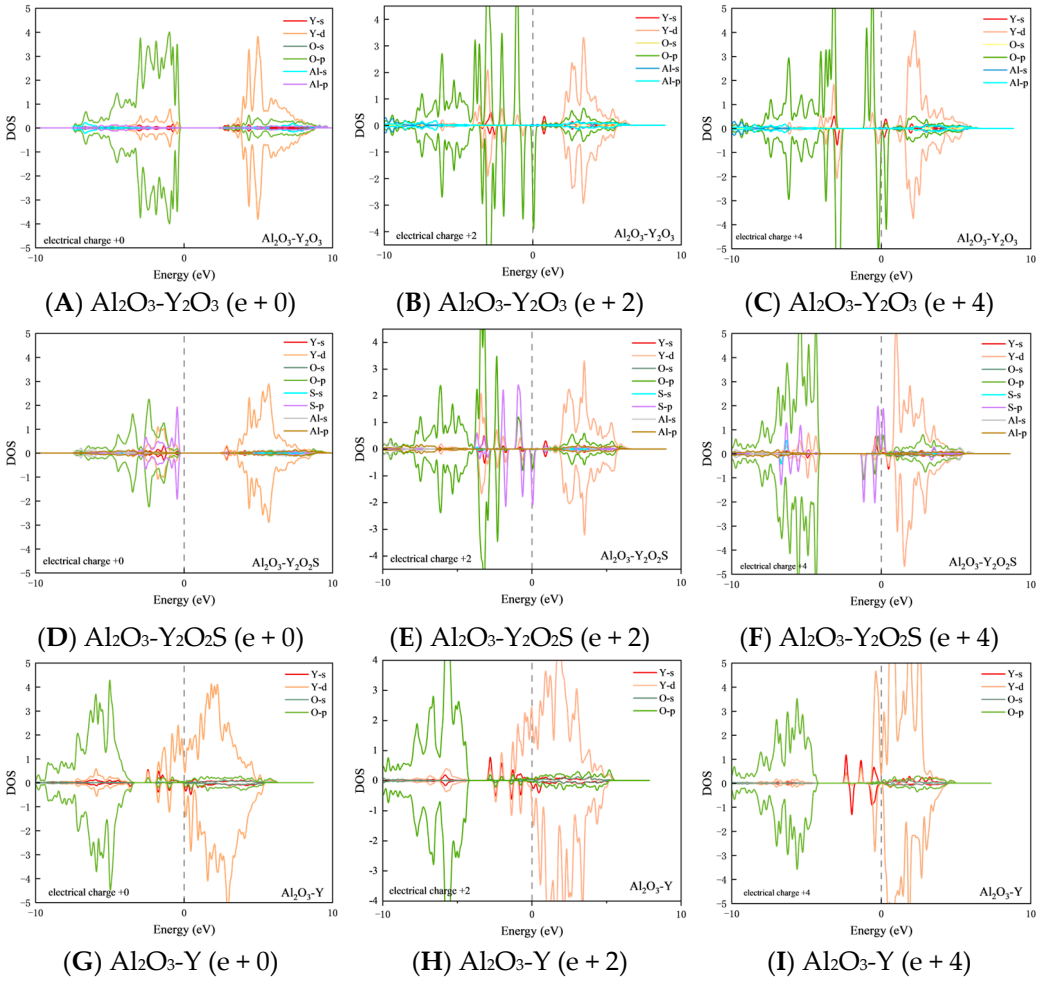


Figure 11. Partial density of states of Al_2O_3 adsorption system. (**A**–**C**) are the partial density of states of Y_2O_3 adsorbed on Al_2O_3 with external charges of +0, +2 and +4. (**D**–**F**) are the partial density of states of Y_2O_2S adsorbed on Al_2O_3 with external charges of +0, +2 and +4. (**G**–**I**) are the partial density of states of Y adsorbed on Al_2O_3 with external charges of +0, +2 and +4.

As the applied positive charge further increases to +4, the reorganization of the electronic structure is more pronounced. In the occupied state region, the localization characteristics of the PDOS peaks are further enhanced, but the orbital overlap between O-p and Y-d is significantly weakened, energy matching deteriorates, and the hybridization intensity decreases sharply, indicating that the original Y-d/O-p chemical bond tends to break. In the antibonding (unoccupied) region, the contribution of the Y-d orbital almost disappears, indicating that it has been "hollowed out". Meanwhile, the fluctuations of

Y-s and O-p orbitals tend to be synchronized, indicating that Y-s/O-p hybridization has become the dominant mode of interface bonding, forming new stable chemical bonds. The energy gap is further narrowed, which is mainly reflected in the downward shift in the conduction band minimum; especially, the new Y-s peak shifts noticeably toward lower energies, indicating that the conduction band bottom has been dominated by the newly formed s-p hybrid antibonding state.

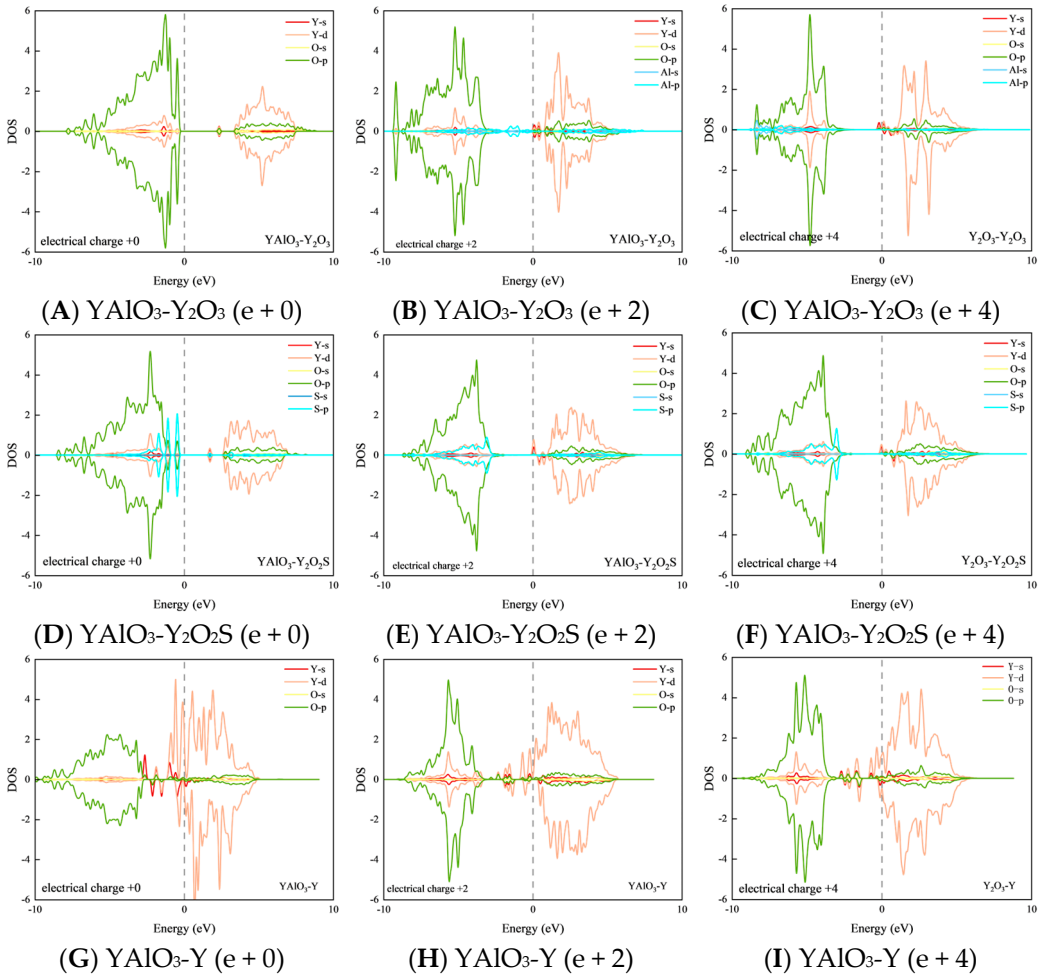


Figure 12. Partial density of states of $YAlO_3$ adsorption system. (**A**–**C**) are the partial density of states of Y_2O_3 adsorbed on $YAlO_3$ with external charges of + 0, + 2 and + 4. (**D**–**F**) are the partial density of states of Y_2O_2S adsorbed on $YAlO_3$ with external charges of + 0, + 2 and + 4. (**G**–**I**) are the partial density of states of Y adsorbed on $YAlO_3$ with external charges of + 0, + 2 and + 4.

In summary, the applied positive charge induces the s-orbital energy level to shift downward by increasing the effective nuclear charge of the Y atom, inducing hybridization with the substrate O-p orbitals to form a lower energy s-p hybrid state, thereby driving the interface bonding mode to change from d-p-dominated to s-p-dominated. This process is accompanied by changes in orbital hybridization intensity, adjustments in energy band structure and the redistribution of interface charge, which demonstrates that substantial electron orbital overlap and charge sharing exist between Al_2O_3, $YAlO_3$ and Y_2O_3 and Y_2O_3 and Y_2O_2S or Y atoms in steel, and that the interface bonding has a clear electronic structure basis.

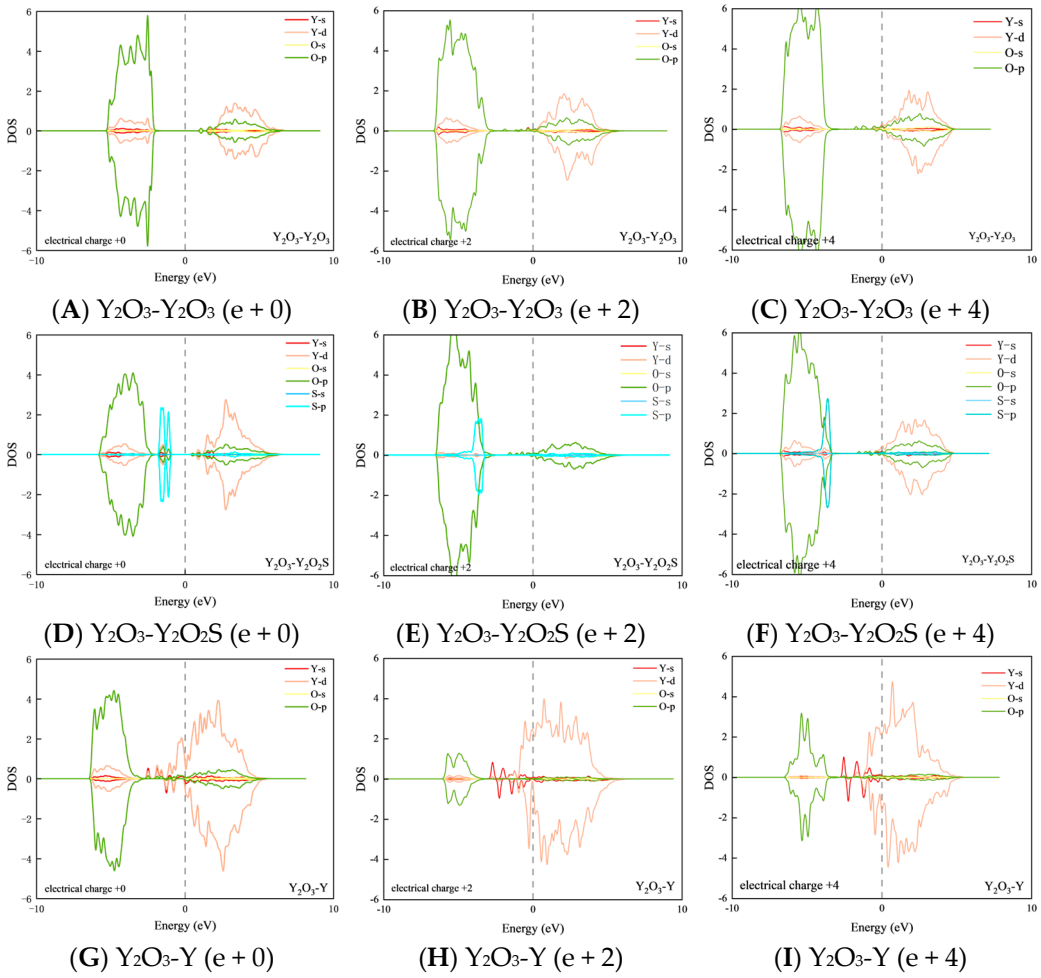


Figure 13. Partial density of states of Y_2O_3 adsorption system. (**A**–**C**) are the partial density of states of Y_2O_3 adsorbed on Y_2O_3 with external charges of +0, +2 and +4. (**D**–**F**) are the partial density of states of Y_2O_2S adsorbed on Y_2O_3 with external charges of +0, +2 and +4. (**G**–**I**) are the partial density of states of Y adsorbed on Y_2O_3 with external charges of +0, +2 and +4.

3.6. Dynamic Adsorption Behavior Under Applied Charge

The temporal evolution of adsorbate population at the refractory–inclusion interface reveals a clear dependence on the substrate charge state (Figure 14). Across all investigated systems (A–I), the adsorption kinetics exhibit an initial rapid increase followed by saturation, characteristic of a pseudo-first-order or diffusion-limited adsorption process. Crucially, as the substrate surface charge increases from 0 to +2 and +4, the final equilibrium adsorption number (N_{eq}) systematically decreases, accompanied by a reduction in the adsorption rate constant (k). This trend confirms that surface charging suppresses the adsorption capacity and kinetics of Y-based inclusions (Y, Y_2O_3, Y_2O_2S) on Al_2O_3, $YAlO_3$, and Y_2O_3 substrates. The attenuation in adsorption is more pronounced for ionic or highly polarizable species (Y_2O_2S, Y) than for less charged or more covalent systems, suggesting that electrostatic repulsion dominates the interfacial interaction under positively charged conditions. These findings are consistent with the proposed mechanism that positive surface charge disrupts Y–O orbital hybridization and enhances interfacial repulsion, thereby thermodynamically and kinetically disfavoring adsorption.

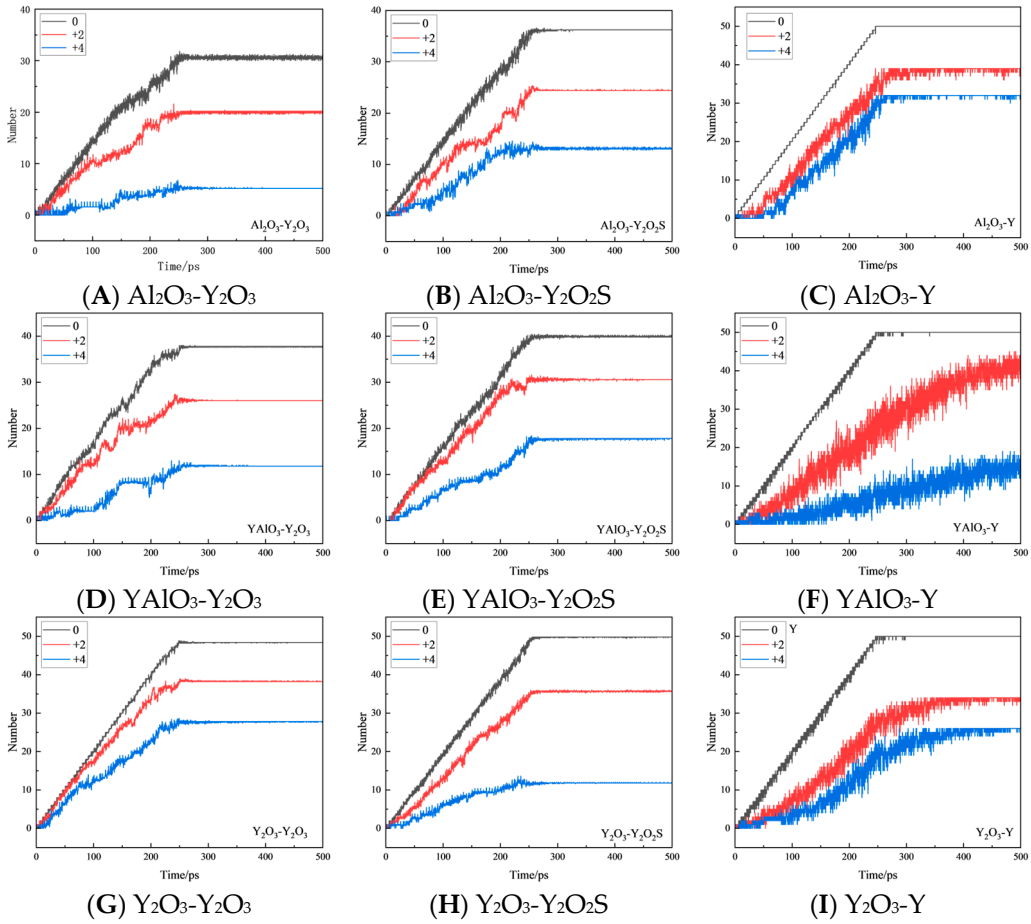
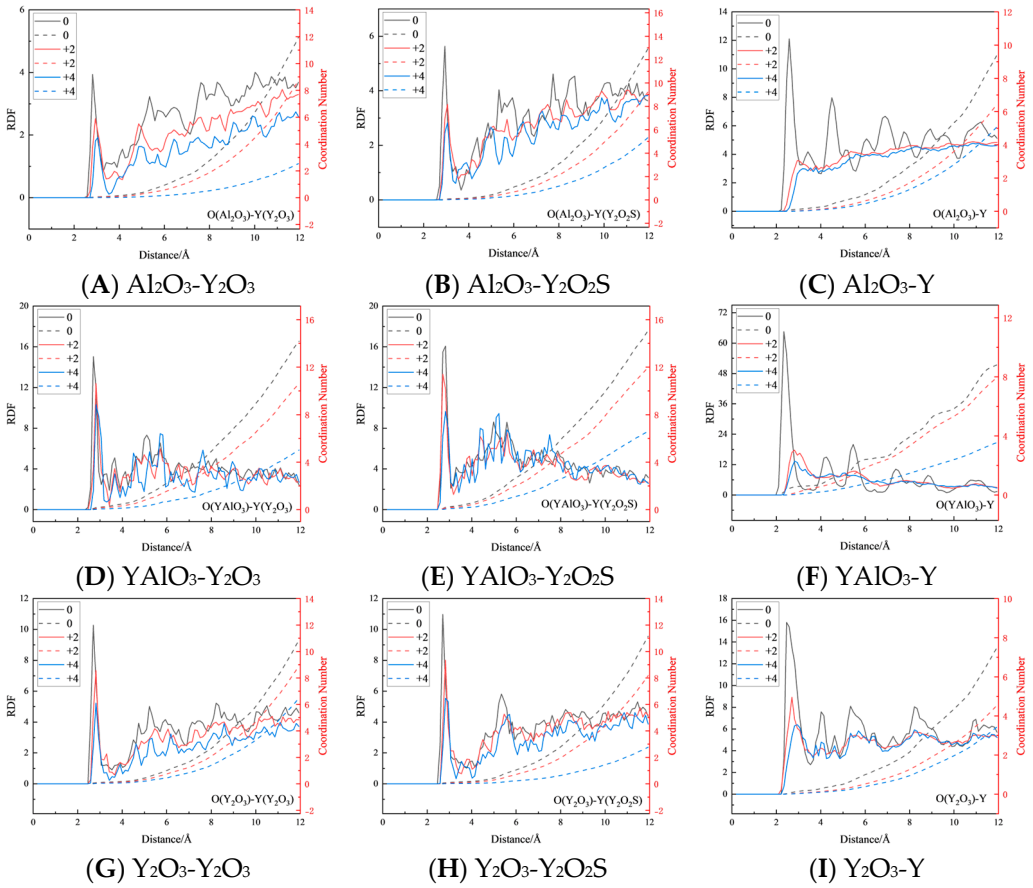


Figure 14. The curve of the number and time of adsorbate at the interface. (**A**–**C**) are the adsorption capacity curves of Y_2O_3, Y_2O_2S and Y atoms adsorbed by Al_2O_3 under the external charge of +0, +2 and +4. (**D**–**F**) are the adsorption capacity curves of Y_2O_3, Y_2O_2S and Y atoms adsorbed by $YAlO_3$ under the external charge of +0, +2 and +4. (**G**–**I**) are the adsorption capacity curves of Y_2O_3, Y_2O_2S and Y atoms adsorbed by Y_2O_3 under the external charge of +0, +2 and +4.

As shown in Figure 15 (panels A–I), increasing the substrate charge from 0 to +2 to +4 induces a universal and monotonic attenuation of interfacial correlation. Specifically, the first peak in the O–Y RDF, corresponding to the primary bonding distance (~2.5 Å), exhibits a systematic decrease in intensity accompanied by peak broadening, while the integrated CN curve shifts downward, indicating a reduction in the average number of O atoms coordinating each Y atom at the interface. This structural evolution provides direct evidence for the weakening of interfacial bonding under positive charging, consistent with the thermodynamic (increased ΔG) and kinetic (reduced adsorption number) findings. Mechanistically, the positive surface charge repels the electropositive Y atoms, increasing the mean O–Y distance and lowering the probability of stable coordination (electrostatic repulsion), while the inhibition of Y–d and O–p orbital hybridization translates into a loss of covalent bond directionality and structural order (peak broadening). The combined effects result in the coordinative unsaturation of interfacial Y atoms, which destabilizes the adsorbed complex and facilitates desorption.



(**A**) Al_2O_3-Y_2O_3 (**B**) Al_2O_3-Y_2O_2S (**C**) Al_2O_3-Y

(**D**) $YAlO_3$-Y_2O_3 (**E**) $YAlO_3$-Y_2O_2S (**F**) $YAlO_3$-Y

(**G**) Y_2O_3-Y_2O_3 (**H**) Y_2O_3-Y_2O_2S (**I**) Y_2O_3-Y

Figure 15. The radial distribution function (RDF) and coordination number (CN) of the O-Y particle pairs of the system. (**A**–**C**) are the radial distribution function and coordination number of Y_2O_3, Y_2O_2S and Y atoms adsorbed by Al_2O_3 under the external charge of +0, +2 and +4. (**D**–**F**) are the radial distribution function and coordination number of Y_2O_3, Y_2O_2S and Y atoms adsorbed by $YAlO_3$ under the external charge of +0, +2 and +4. (**G**–**I**) are the radial distribution function and coordination number of Y_2O_3, Y_2O_2S and Y atoms adsorbed by Y_2O_3 under the external charge of +0, +2 and +4.

4. Conclusions

In this study, combining partial density of states analysis, charge density difference calculation and high-temperature thermodynamic simulations, we systematically reveal the inherent mechanisms of external charge-induced interfacial adsorption inhibition from three aspects: electronic structure evolution, interfacial bonding mechanism and macroscopic thermodynamic behavior. We also construct a complete regulation pathway "charge loading → orbital hybridization attenuation → electrostatic environment repulsion → reactive activity inhibition → adsorption driving force loss".

1. Based on the DFT calculations, the applied charge weakens the electronic foundation of interfacial bonding. In the neutral adsorption state, there is a good energy matching and peak alignment between the Y-d orbital and the substrate O-p orbital, which constitute the electronic origin of covalent bonding. With the introduction of positive charge, the overlap region of the two in PDOS shrinks significantly, the orbital hybridization intensity decreases, the nucleophilicity of oxygen atoms on the substrate surface is inhibited, and the interfacial charge transfer efficiency is significantly reduced, resulting in the systematic weakening of the bonding strength within our computational model, and the adsorption reaction loses the original electron-driven foundation.

2. The calculations indicate that the external charge significantly changes the electrostatic environment of the interface. The charge density difference analysis shows that the electrons migrate from the substrate to the adsorbate under neutral conditions, forming an electrostatic attraction. Under a positive charge background, the system as a whole exhibits a net positive charge, which exerts a significant Coulomb repulsion effect on the Y-type adsorbate with the same positive charge, and the negative charge of the substrate oxygen atoms also decreases significantly. The electrostatic interaction changes from attraction to repulsion, which, according to our results, forces the adsorbate to overcome a higher energy barrier upon approaching the interface.
3. The external charge significantly increases the thermodynamic barrier of the adsorption process. The thermodynamic calculation results show that the Gibbs free energy change ΔG in the adsorption reaction is significantly higher than that in the neutral state in the +2 and +4 charge states, and the adsorption driving force exhibits a systematic decrease. The fundamental reason is that the applied charge disrupts the bonding strength of the interface, resulting in the adsorption reaction losing its primary energetic driving force. In the high-temperature range of 1473–1873 K, this bonding disruption effect dominates, far exceeding the thermodynamic gain from entropy increase, and becomes the key mechanism to achieve adsorption inhibition.
4. The calculations indicate that the inhibition effect of the applied charge may be broadly applicable across different systems while maintaining controllability. Whether the adsorbed species are Y_2O_3 and Y_2O_2S or Y atoms, and whether the substrate material is Al_2O_3, $YAlO_3$ and Y_2O_3, the positive charge application is observed to consistently reduce the interfacial adsorption strength and reactivity in our calculations. This finding indicates that could be a widely applicable strategy to inhibit undesired adsorption and interface reaction by regulating the local charge state of the interface, which provides a theoretical basis for the designing of electrochemical anti-adhesive interfaces.
5. AIMD simulations at 1830 K reveal that increasing the substrate charge from 0 to +2 to +4 systematically reduces both the equilibrium adsorption number and the adsorption rate constant of *Y*-based inclusions on Al_2O_3, $YAlO_3$ and Y_2O_3 surfaces. Radial distribution and coordination number analyses show decreased Y-O peak intensity and coordination, indicating weakened interfacial bonding due to electrostatic repulsion and suppressed orbital hybridization. These dynamic findings corroborate the static DFT thermodynamic trends and collectively establish a multi-level mechanism by which positive surface charge inhibits adsorption through electronic, electrostatic, and kinetic pathways.

Future work should validate the proposed inhibition mechanism under more realistic conditions. Experimentally, techniques such as spectroscopy, X-ray photoelectron spectroscopy (XPS), or transmission electron microscopy (TEM) can be employed to confirm the charge-induced suppression of inclusion adhesion. Computationally, further refinement may include surface defects, the molten steel environment, and constant potential methods to better represent the electrochemical interface. Bridging the gap between idealized models and industrial applications remains a key objective.

Author Contributions: Conceptualization, methodology, software, verification, data management, writing—review and editing, visualization, X.Z.; data curation, software, D.L.; funding acquisition, project administration, C.L.; supervision, H.W.; supervision, C.P. All authors have read and agreed to the published version of the manuscript.

Funding: This work was supported by the National Science Foundation of China (Grant No. 52374337), the National Key R&D Program of China (Grant No. 2022YFC2905205), the Jiangxi Provincial Natural Science Foundation (Grant Nos. 2025BAC200310, 20232BAB204002), and the Doctoral Scientific Research Foundation of Jiangxi University of Science and Technology No. 205200100601.

Data Availability Statement: The data presented in this study are contained within the article. Further inquiries can be directed to the corresponding authors.

Conflicts of Interest: The authors declare no conflicts of interest.

References

1. Gong, A. The role of rare earths on steel and rare earth steel corrosion mechanism of research progress. *Coatings* **2024**, *14*, 465. [CrossRef]
2. Zeng, B.; Zheng, Q.; Li, G.Q.; Zhao, Y.J.; Liu, Y.; Yuan, C.; Meng, Z. Comparative study on interaction between rare earth oxide refractories and rare earth treated steel. *J. Iron Steel Res.* **2024**, *31*, 1493–1501.
3. Luan, Y. Preparation of low-oxygen rare earth bearing steel and high-end bearings. *China Rare Earth Inf.* **2024**, *30*, 3–8.
4. Jiang, X.; Zhang, Z.M.; Luo, D.Q.; You, J.; Lai, C. Structural stability and thermodynamic properties of $(Y_2O_3)n(n=1-15)$ clusters based on density functional theory. *Int. J. Quantum Chem.* **2021**, *121*, e26802. [CrossRef]
5. Luo, D.; Yu, Y.; Zhang, Z.M.; Sun, L.; Feng, X.; Lai, C. Development of high impact toughness offshore engineering steel by yttrium-based rare earth addition. *Ironmak. Steelmak.* **2021**, *48*, 1247–1253. [CrossRef]
6. Meng, D.; Nandipati, S.B.; Silaen, A.K.; Wang, Y.; Abraham, S.; Brown, D.; Zhou, C. Impacts of cooling reduction due to spray nozzle clogging on shell formation in continuous casting of steel. *Metals* **2025**, *15*, 1107. [CrossRef]
7. Hua, C.; Wang, M.; Senk, D.; Wang, H.; Zhang, Q.; Zhi, J.; Bao, Y. Cone clogging of submerged entry nozzle in rare earth treated ultra-low carbon Al-killed steel and its effect on the flow field and vortex in the mold. *Metals* **2021**, *11*, 662. [CrossRef]
8. Yang, W.; Zhang, L.; Ren, W.L.F. Formation and prevention of nozzle clogging during the continuous casting of steels: A review. *ISIJ Int.* **2024**, *64*, 1–20. [CrossRef]
9. Wang, H.; Wang, J. Study on the Mechanism and control of clogging growth on the submerged entry nozzle of Q355 steel. *Steel Res. Int.* **2025**, *96*, 2400514. [CrossRef]
10. Wang, J.; Xia, M.; Wu, J.; Ge, C. Ladle Nozzle Clogging in Vacuum Induction Melting Gas Atomization: Influence of the Melt Viscosity. *Metall. Mater. Trans. B* **2022**, *53*, 2386–2397. [CrossRef]
11. Qin, J.; Liu, D.F.; Yue, Y.; Zhao, H.J.; Lai, C.B. Effect of normalization on texture evolution of 0.2 mm-thick thin-gauge non-oriented electrical steels with strong η-fiber textures. *J. Iron Steel Res.* **2019**, *26*, 1219–1227. [CrossRef]
12. Xi, X.J.; Yang, S.F.; Li, J.S.; Luo, D.Q.; Cai, X.N.; Lai, C.B. Phosphorus distribution between rare earth oxides containing slags and ferromanganese alloy. *Ironmak. Steelmak.* **2019**, *46*, 485–490. [CrossRef]
13. Xi, X.J.; Luo, D.Q.; Cai, X.N.; Lai, C.B. Dephosphorisation of ferromanganese alloy using rare earth oxide-containing slags. *Can. Metall. Q.* **2018**, *57*, 493–500. [CrossRef]
14. Goto, K.; Ling, L.; Matsumoto, S.; Morikawa, K.; Sasaki, A. Development of new ZrO_2-CaO-C material for high-performance anti-clogging nozzle. In Proceedings of the AISTech 2024—Proceedings of the Iron & Steel Technology Conference, Columbus, OH, USA, 6–9 May 2024; pp. 1038–1048.
15. Chen, K.; Wang, D.; Yuan, L.; Gu, Q.; Liu, G.; Li, H. A novel method for suppressing clogging of nozzle and stopper rod by electric current pulse during continuous casting of ultra-low carbon steel. *J. Manuf. Process* **2025**, *151*, 1–23. [CrossRef]
16. Svensson, J.K.S.; Larsson, F.; Memarpour, A.; Ekerot, S.; Brabie, V.; Jönsson, P.G. Implementation of an YSZ coating material to prevent clogging of the submerged entry nozzle (SEN) during continuous casting of Ce-treated steels. *Ironmak. Steelmak.* **2018**, *45*, 105–113. [CrossRef]
17. Srinivas, P.S.; Mishra, D.K.; Gupta, R.; Korath, J.M.; Jana, A.K. Vortex characteristics due to nozzle clogging in water caster mould: Modelling and validation. *Can. Metall. Q.* **2019**, *58*, 308–324. [CrossRef]
18. Yang, W.; Luo, Z.; Gu, Y.; Liu, Z.; Zou, Z. Numerical Analysis of Effect of Operation Conditions on Bubble Distribution in Steel Continuous Casting Mold with Advanced Bubble Break-up and Coalescence Models. *ISIJ Int.* **2021**, *73*, 3910–3919. [CrossRef]
19. Tian Chen, Y.; Jin, J.K.; Wen, E.D. Effect of interfacial reaction behavior on the submerged entry nozzle by the electric current pulse. *J. Alloys Compd.* **2019**, *809*, 151825. [CrossRef]
20. Yan, L.G.; Chen, L.; Liu, C.H.; Pang, S.; Zhang, X.; Zhang, L. Intervening interfacial reaction between refractory and rare earth-bearing molten steel by pulsed electric current to inhibit the clogging of submerged entry nozzle. *J. Manag.* **2021**, *73*, 3910–3919. [CrossRef]
21. Yu, W.W.; Qi, J.G.; Cui, H. Pulsed electric current treatment: From regulating non-metallic inclusions to inhibiting submerged entry nozzle clogging. *J. Iron Steel Res.* **2025**, *32*, 833–848. [CrossRef]

22. Jiang, X.; Luo, D.; Zhang, Z.; Liu, M.; Liu, Y.; Yu, Y.; Feng, X.; Lai, C. Multiscale nucleation growth model of yttrium oxide during the deoxidation of Fe–O–Y melt. *J. Mater. Sci.* **2021**, *57*, 6988–7000. [CrossRef]
23. Tian, C.; Yuan, L.; Yu, J.; Jia, D.; Wen, T. Effect of an external electric field on the wall of a rare earth steel submerged entry nozzle. *J. Mater. Res. Technol.* **2021**, *11*, 404–411. [CrossRef]
24. Lousada Cláudio, M.; Brinck, T.; Jonsson, M. Application of reactivity descriptors to the catalytic decomposition of hydrogen peroxide at oxide surfaces. *Comput. Theor. Chem.* **2015**, *1070*, 108–116. [CrossRef]
25. Mazumder, A.; Alangi, N.; Sethi, S.; Prabhu, K.N.; Mukherjee, J. Study on wettability of plasma spray coated oxide ceramic for hydrophobicity. *Surf. Interfaces* **2020**, *20*, 100591. [CrossRef]

Disclaimer/Publisher's Note: The statements, opinions and data contained in all publications are solely those of the individual author(s) and contributor(s) and not of MDPI and/or the editor(s). MDPI and/or the editor(s) disclaim responsibility for any injury to people or property resulting from any ideas, methods, instructions or products referred to in the content.